Supplement of Atmos. Chem. Phys., 21, 1987–2001, 2021
https://doi.org/10.5194/acp-21-1987-2021-supplement

Atmospheric Chemistry and Physics
Open Access
EGU

Supplement of

Measurement report: Sulfuric acid nucleation and experimental conditions in a photolytic flow reactor

David R. Hanson et al.

Correspondence to: David R. Hanson (hansondr@augsburg.edu)

S1.Apparatus overview

PhoFR is a jacketed flow reactor with 5.0 cm inner diameter, with 113 cm of its length illuminated by 4 BLB fluorescent bulbs. Most gas inlets are located in a conical region partitioned from the main flow reactor by a Teflon mesh (~ 0.5 mm x 0.5 mm openings); an inlet for introducing amino-compounds to the flow is located just below this mesh. A phosphoric acid coated 80 cm length of tubing – along with a thin strip of Teflon mesh to maintain acid spreadout – was installed on the exit of the dry N_2 flow meter (23Aug2019). Algae accumulation inside the cooling jacket was almost completely removed (alcohol - KOH soak) in Dec2019. Neither of these actions had noticeable effects on the temporal trends in experimental results.

S1.1 Particle counters

The second particle counter is the UCPC system used in Zollner et al. [2012] which is nearly identical to that described by Stolzenburg and McMurry [1981]. The new working conditions for this instrument presented by Kuang et al. [2012] was used for the work here: saturator temperature of 45 C, condenser temperature 10 C, condenser flow of 10 cm^3/s (0.6 Lpm) and a capillary flow of 1.2 cm^3/s. The 50% cutoff diameter for these UCPC conditions is ~2 nm. A transport flow of 0.3 Lpm was used for the majority of the measurements, due to limitations of the total flow in the experiment. The effect of transport flow on the UCPC count rate is shown in Fig. S1 below (the 0.6 lpm data was collected with a decreased DEG transport flow.)

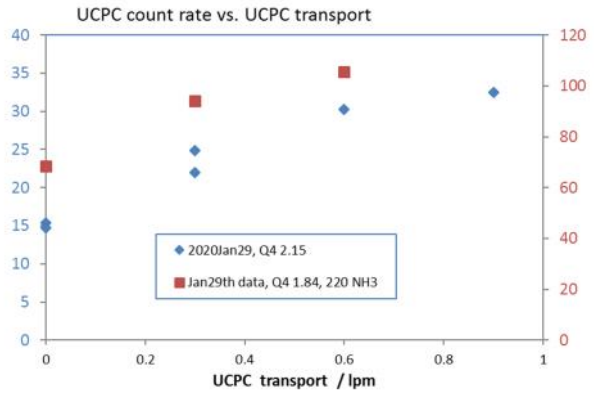

Fig. S1. Count rate (uncorrected raw numbers) of the UCPC vs. UCPC transport flow rate. Particle size was nominally 3.1 nm diameter for each set of data. Experimental conditions for red squares, Q_4=1.84 sccm, 220 ppt NH_3 added (right axis); blue diamonds, Q_4=2.15 sccm, no added NH_3 (left axis).

The particle counters' dependencies on operating conditions are documented for efficiencies [Stolzenburg and McMurry, 1980; Kuang et al. 2012; Kangasluomo et al., 2014] and the nano-DMA is a standard device (TSI model 3085) and the data is analyzed accordingly. We note that background count rates are monitored for every run. We have not formally calibrated either counter. In the next section is a direct comparison of them using small seed particles indicating agreement generally better than 50%.

S1.1.1 Comparison of N_p from the two particle counters: Seed particles.

The number densities of externally generated nano-particles were monitored with both the UCPC instrument and the DEG system, the initial distribution and also with growth in PhoFR. These nano-particles are characterized by a well-defined log-normal mode and are therefore provide a good test for the calculated size-dependent counting efficiencies

of the two systems. Shown in the three plots below are the N_p for three different experiments. There is generally good agreement across the size range indicating an absence of: (i) a persistent, concerning, systematic bias between the counters and (ii) a bias in their size-dependent counting efficiencies. One set of experiments reveals a consistent bias of about plus 30 % for the UCPC data for which the cause is unknown; yet it is not to a level that is a critical concern at this time. Note that nucleated N_p for both counters was generally elevated throughout March of 2020 (see next section.)

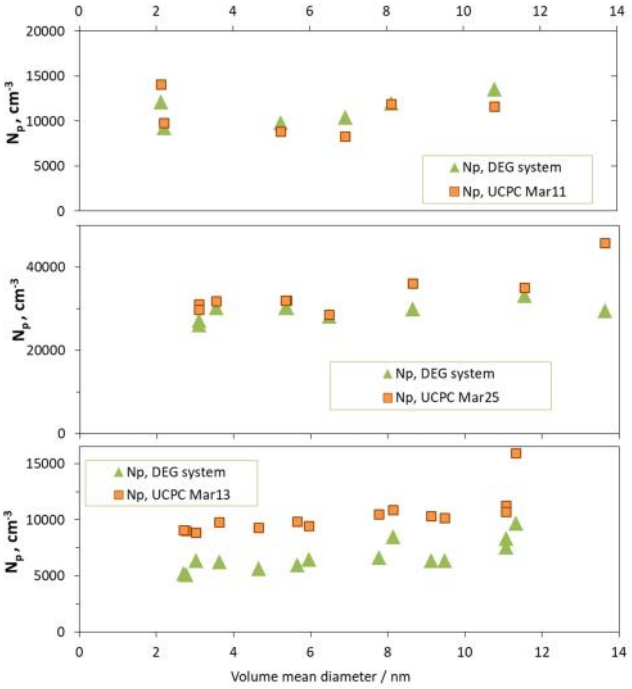

Figure S2. Variation of N_p from the two counters as a function of particle diameter. Particles were generated in a separate flow reactor and then either passed through or were grown in PhoFR with size determined by the HONO-level. See Fig S5 below for typical size distributions.

S1.1.2 N_p for UCPC and DEG over time.

The nucleation data from the two counters for Q_4 = 4.2 sccm are plotted over time in Fig. S3. During March of 2020, N_p from both particle counters was elevated, the onset of which was simultaneous with a gas source change. In this month, the perturbation to the UCPC numbers was greater than that to the DEG numbers. The gas source changes in late Jan and mid-April did not initiate the same behavior in the instruments and the UCPC N_p was always lower than the DEG N_p.

We presented evidence in section 3.4 that ion-mediated processes could lead to large artifacts in the DEG N_p that the UCPC is relatively immune to. Other factors that could lead to differences in N_p from the two counters include (i) changes in how the sampling flow was split between the instruments, (ii) restricting DEG N_p to the leading edge particles, and (iii) differences in response to particles formed in episodic contamination events. For (i), the flow splits at a ¼" Swagelok tee with the UCPC sampling straight and the DEG taking its flow at right angles: early experiments showed small differences when the DEG sampled the straight leg, however, more targeted work is needed. For (ii), small particles in the DEG distributions can number as much as, or greater than, those in the leading edge. Definitive statements about counter biases due to (iii) are not possible at this time but we note that charging probabilities and activation efficiencies are two factors that can depend on particle size and composition. Nonetheless, both sets of N_p data are much lower than our previous results [Hanson et al. 2019].

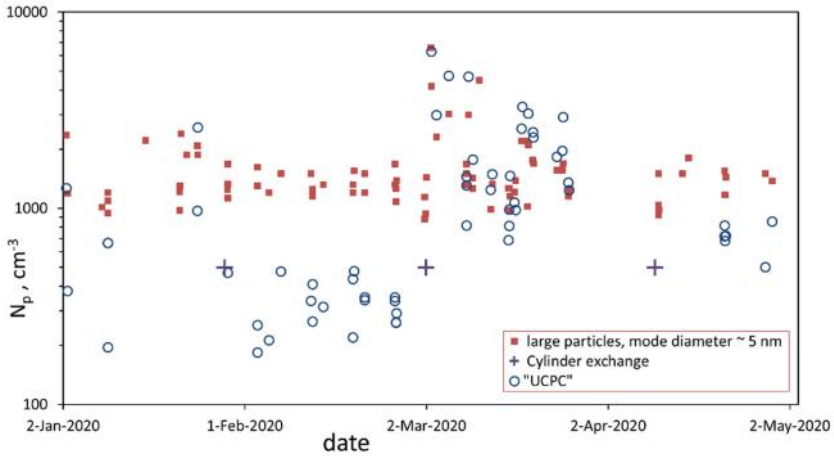

Fig. S3. Comparison of Np from nucleation experiments in PhoFR for both counters over several months for Q_4=4.2 sccm. The DEG N_p are plotted as red squares and UCPC N_p as circles (with + indicating cylinder changes.)

S1.2 External particles grown in PhoFR.

Additional experimental results are presented here for the growth of nanoparticles introduced at the top of PhoFR as a function of Q_4, the flow through the HONO source. The particle size distribution volume-weighted diameter is plotted vs. Q_4 in Figs. S4 and the particle's initial size is indicated at Q_4 = 0 (determined from the lights off measurements.) Shown in Fig. S5 are the size distributions for one set of measurements.

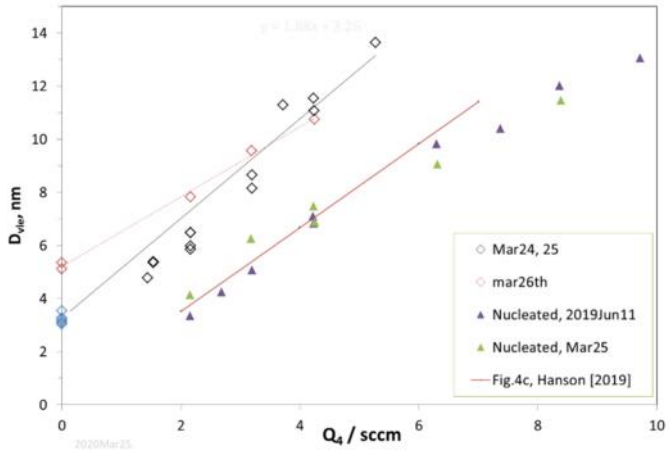

Fig. S4. Volume-weighted diameter of particles vs. Q_4, the HCl-laden N_2 flow through the HONO source. Data at Q_4=0 are the initial size of the nanoparticles (with photolysis suspended). For 2020Mar24 and 25, N_p for the seed particles was $3x10^4$ cm^{-3}. The growth slope (black line) is somewhat larger than the nucleation slope (red dashed line). The green and purple triangles are sizes of nucleated particles in PhoFR from 2020Mar25 and 2019Jun11. Mar 26 was with nanoparticles produced in BFR with ammonia at 1.3 ppbv. The growth slope is lower for this set of data. The nanoparticles are more numerous ($2.6x10^5$ cm^{-3}) and their size distributions were not well-described by a single log-normal (see Fig. S5b).

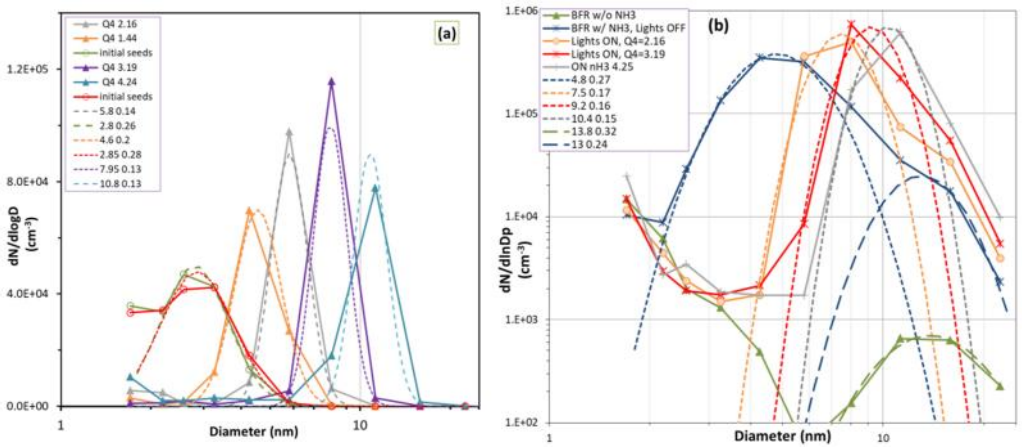

Fig. S5. Size distributions of externally-generated seed particles and after they were grown. (a) Size distributions of 24Mar2020 data at different HONO flows, Q_4, indicated in the legend along with log-normal fits and parameters; lights OFF distributions are in green and red. Seed particles generated in BFR (Glasoe et al.) with 15 ppt DMA and a very low total flow (1.5 sLpm). (b) Growth plots for 26Mar2020 with 1.3 ppb NH_3 in BFR to induce seed particle formation: note the two modes. The size distribution of seed particles generated in BFR without NH_3 added is also shown.

S1.3 UCPC and DEG N_p as a function of SO_2.

Three sets of calculations and two sets of experimental data are shown in Fig. S6 where SO_2 was varied (Q_1 is flow of the 1% SO_2 in air mixture) at Q_4 = 4.2 sccm. The model results, using the present NH3_D52 (aka D52octo) thermodynamics, for zero ammonia (purple line) and 25 pptv ammonia (orange line) do not describe the data very well. If a strong nucleating agent that acts like dimethylamine is present at 10^{-16} mole fraction, the model results with DMA_I free energies [Hanson et al. 2017] results best approximate the lack of a dependence on SO_2 in the data.

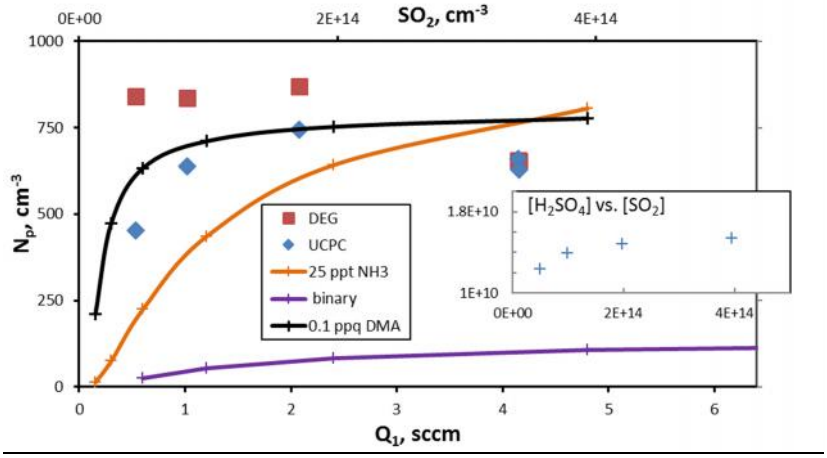

Fig. S6. Variation of N_p with SO_2 mixture flow rate at Q_4 = 4.2 sccm. A flow rate of 1 sccm of the 1 % SO_2 mixture is a number density $[SO_2]$ of $8.6x10^{13}$ cm^{-3}. The previous PhoFR data showed a large effect on SO_2 with N_p increasing from 7000 cm^{-3} to 30000 cm^{-3} over the range of SO_2 in Fig. S6. Inset shows calculated on-axis $[H_2SO_4]$ at 120 cm as a function of $[SO_2]$. Calculations for binary and 25 ppt NH_3 used NH3_D52 free energies and 0.1 ppq DMA used DMA_I free energies.

S1.4 N_p and mode diameter vs. Q_4 over time.

Shown in Fig S7 are the leading edge particle's number density N_p and mode diameter vs. Q_4. The data has been split into four time periods to illustrate the change over time in the relationship between the measurements and Q_4. The

2018 May and June data were included in the Hanson et al. [2019] data set (a $Q_4^{3.5}$ power relationship is shown in (a)), the 29Jun2028 to 28Sep2018 data largely overlaps the earliest data, while the Oct2018 data (red squares) departs to lower N_p at all Q_4 while mode diameter seems to be a little larger than the other data. Aside from this and despite the scatter in the mode diameter data, there is not a temporal trend in particle growth over time, suggesting that HONO and NO levels were relatively constant.

We are suggesting that, since the flow reactor is believed to be cleaner than it was in early 2018, the onset of nucleation for the majority of the large particles has moved down the flow reactor to perhaps 60 cm. This would lead to less H_2SO_4-exposure and therefore less growth, about 15 %, which in principle could be discerned in the leading-edge measurements. The quadratic fits shown in Fig. S7(b) indicate there is not a change of this amount yet the scatter of the data is large.

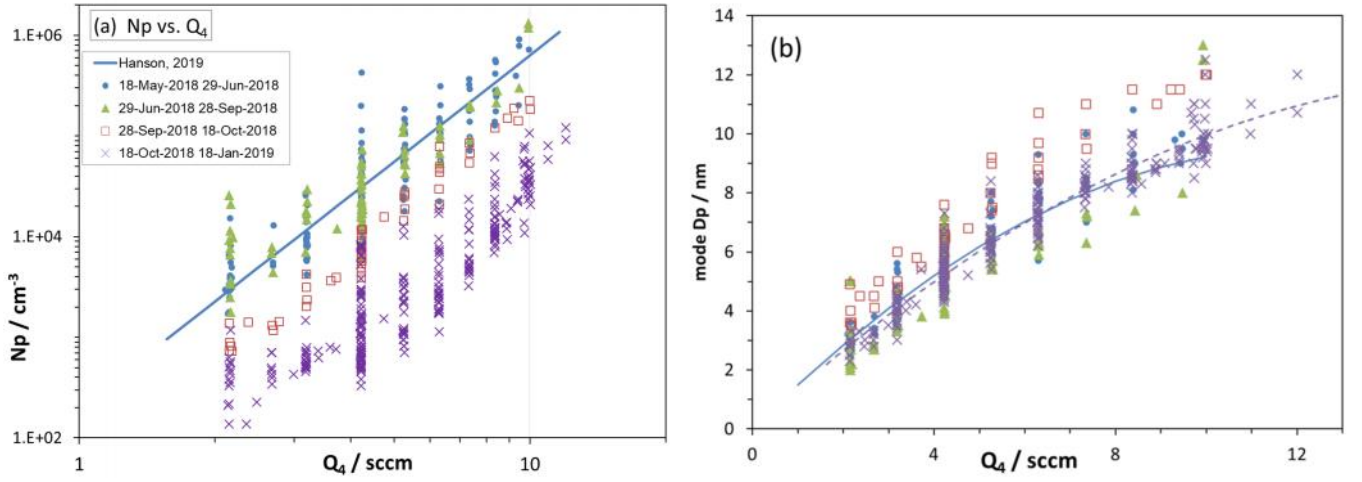

Fig. S7. Particle characteristics, (a) Np and (b) mode diameter, of the leading edge mode from the DEG system vs. Q_4. Data for N_p in blue was published in Hanson et al. [2019]; a new quadratic fit to the mode diameter for this period is included as the blue line in (b). The latest set of data in (b) was also fit to a quadratic (purple dashed line); these fits are meant to facilitate comparison between the two time periods.

S1.5 Sensitivity to room temperature.

An example of an incident where a fluctuation in the temperature sensor mounted on the top cone (T_{cone}, red line) affected the UCPC count rates and the DEG system measurements (raw count rates for several voltages sent to the nano-DMA are shown). Fluctuations in this temperature of 0.4 ^oC result in noticeable changes in the count rates for both the UCPC and DEG system.

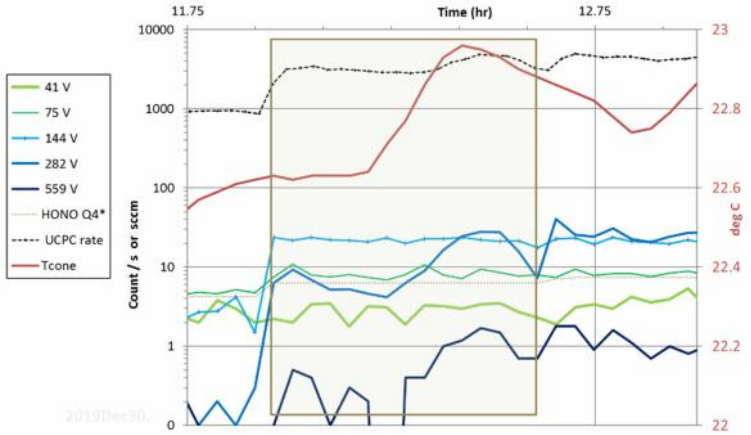

Fig. S8. Plots of particle detector count rates (left axis) and T_{cone} (right axis) vs. time. The gold box highlights the data while Q_4 was constant at 6.3 sccm. The first five labels in the legend are the DEG count rates at selected voltages (the labels) sent to the nanoDMA, the UCPC count rate is the dashed black line.

Attempts to induce effects on N_p by intentionally varying T_{cone} were not conclusive. We think changes in T_{cone} are a proxy for changes in the temperature of the room that may have affected the temperature of other parts of the apparatus, such as the reservoirs and delivery lines for the HONO source.

S1.6 NO_x and NO measurements.

Shown in Fig. S9 are the mixing ratios of NO_x and the percent as NO in the HONO source flow, Q_4. There is quite a bit of scatter in the NO fraction for the time period 05July2019 to 04Nov2019 with a relatively high average NO fraction of 20 % of the measured NOx. Late in the day 04Nov2019, the NaONO(s) was replaced and the vessel holding it was swapped out for a smaller vessel. The measurements after that generally had lower NO levels presumably due to less HONO decomposition. The DEG CPC became increasingly noisy in the first four months of 2020 and it was replaced with a second butanol-based CPC system in May of 2020 (the filled red squares in the figure). This CPC system is known to efficiently detect 3 nm and larger particles [Kangasluoma et al. 2014].

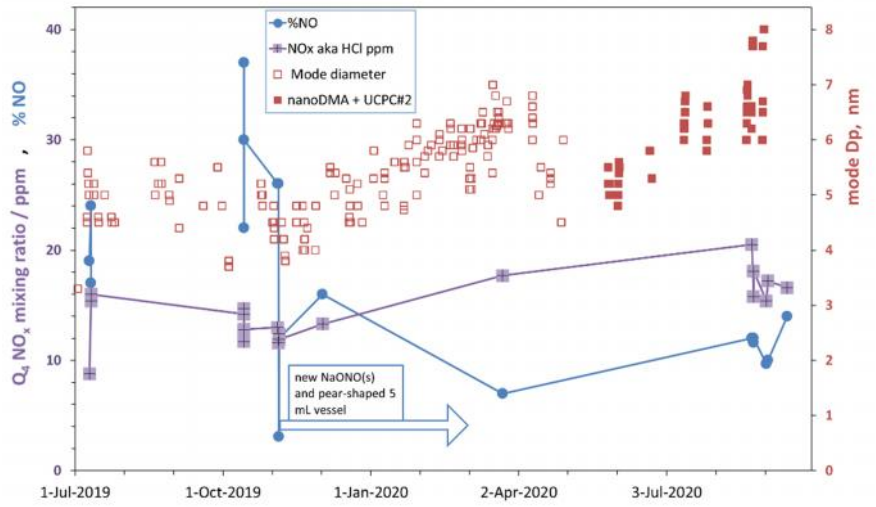

Fig. S9. NO_x and NO measurements and the mode diameter of nanoparticles formed in nucleation experiments as a function of time. Nucleation baseline conditions of Q_4 = 4.2 sccm, 52 % RH, 296 K. Over the period Jul to Dec 2019, NO_x was on average 13 ppmv and NO was 23 % of that while from Mar2020 to Sep2020 NO_x averaged 17 ppmv and NO was on average 11 % of that. Note that the DEG N_p over the time periods Jul2019-Dec2019 (Fig. 1) and Jan2020-Apr2020 (Fig. S3) was about 1500 cm^{-3}. The DEG CPC was replaced with a butanol CPC in the month of May, 2020.

S2. Models.

The model was presented in Hanson et al. [2019] and here significant changes in parameters are detailed. The main differences are in the HONO and NO levels. The most recent measurements of the HCl mole fraction of Q_4 is 17 ppbv (albeit with excursions from this value, see Fig. S9) which was taken from the NO_x measurements (such as Fig. 2); we had estimated 15 ppbv previously. The NO level is taken from measurements such as shown in Fig. 2; NO_2 is taken to be equal to NO and HONO is summarily reduced. The inclusion of initial NO levels from the HONO source is the most consequential difference with our previous model calculations.

No longer included is a reaction between HO_2 and SO_2. It had been invoked to explain the dependence of N_p on SO_2 level in our previous work. This reaction added 10-15 % to the simulated H_2SO_4 production rate. Interestingly, with the inclusion of small amounts of NO and NO_2 coming from the HONO source, the model (either binary or with low levels of added base, Fig. S6) shows a significant dependence on SO_2 level which may be due to SO_2 competing with NO and NO_2 for OH.

There are a few other model details worth re-iterating here. When a base is added, it is constrained to the middle 25 % of the mass-flow (middle fake) to mimic the elevated concentration of the base in the sidearm flow in the experiment. All temperatures are 296 K and laminar flow is assumed. N_p is taken to be the sum of all the truncation clusters at Z=125 cm and R = 0 when clusters were limited to 10 or fewer SA molecules; when growth to larger clusters was simulated, N_p is the sum of all clusters of 10 or more SA molecules.

S2.1 Verification of box-model

In this section we provide a comparison of our model to the nucleation rates from the ACDC model (McGrath et al. 2011) published in Kürten et al. [2016] when 100 pptv of NH_3 is present.

With the thermodynamics set to those of Ortega et al [2012] (with corrigendum for 4a, 3b cluster) and allowing clusters containing 5 sulfuric acid molecules to accumulate, we calculated the nucleation rate, $J_{box\,5}$, of 5 acid clusters. This approach will mimic the nucleation rate used for the ACDC model where the 5a4b and 5a5b clusters were considered stable (the distribution is dominated by these clusters). Please see Hanson et al. [2017] (DOI: 10.1021/acs.jpca.7b00252) section 2.4 and in its supplement S2.1 and S2.4 for additional information on the 0-D (box) model.

Three representative points along the neutral ACDC data presented in Kürten et al. [2016] (green solid line, 278 K, 100 pptv NH_3) were simulated with our box model and the results are compared in Table S1. Results were also obtained for larger sets of clusters: $J_{box\,6}$ and $J_{box\,8}$, see below.

Table S1. Comparison of Box Model nucleation rates with ACDC using Ortega et al. [2012] NH_3-H_2SO_4 thermodynamics, 278 K and 100 pptv NH_3.

$[H_2SO_4]$ (cm^{-3})	J_{ACDC}	$J_{box\,5}$ ($cm^{-3}\,s^{-1}$)	$J_{box\,6}$	$J_{box\,8}$
$9x10^6$	1.0	1.2	0.16	0.016
$1.8x10^7$	10	12	4.4	1.5
$3.8x10^7$	100	112	77	62

At 278 K, evaporation rates of the 5a clusters are significant and this leads to large decreases in the nucleation rates as the size of the system is allowed to increase. The H_2SO_4 content of the accumulation cluster is indicated in the subscripts 5 6 8 in the column titles in Table S1. This was accomplished by assuming a reasonable set of free energies for the 5a 1-5b clusters, thus in the $J_{box\,6}$ and $J_{box\,8}$ calculations, they can evaporate with the accumulation clusters set to all the 6a and 8a clusters ($J_{box\,8}$ also allows 6a and 7a clusters to evaporate). The box model nucleation rates for the 6a accumulation clusters, $J_{box\,6}$, decrease by 32, 64 and 86 % from $J_{box\,5}$ for the three different levels of H_2SO_4, respectively, shown in Table S1. The trend continues as the thermodynamics are further extrapolated allowing for larger accumulation clusters and $J_{box\,8}$ rates decrease another 20, 65, and 90 % from $J_{box\,6}$.

This clearly indicates that the Ortega et al. [2012] NH_3-H_2SO_4 clusters are not large enough for many experimental conditions, particularly for simulations at 278 K and warmer and low sulfuric acid levels. For simulations at 292 K and 100 ppt NH_3 and SA at $1x10^8$ cm^{-3}, the $J_{box\,5}$ nucleation rate is 10.1 cm^{-3} s^{-1} which agrees with ACDC as presented in Kürten et al. Extending the thermodynamics and calculating $J_{box\,6}$ as above, the nucleation rate falls to 1.6 cm^{-3} s^{-1}, which is an 85 % decrease. In fact, one of the main points of our Measurement Report is that the thermodynamics of clusters that contain up to ten acid molecules are needed for describing nucleation in the NH_3-H_2SO_4-H_2O system.

S3. Growth rate calculation.

Sulfuric acid-water nanoparticles' composition is predicted to vary with size (see Table S3 below, Liquid Drop Model [Lovejoy et al. 2004; Yu et al. 2005]) and therefore the Verheggen and Mozurkewich [2002] approach, where the particle's volume is differentiated with respect to time, is a good starting point. After we modify it by including some terms and rearranging it, we will integrate it from 2.2 to 8.7 nm (geometric or mass diameter.) This equation is readily modified to account for the vapor molecule's size (parenthetical term in S1) and for the particle–vapor reduced mass (in the mean molecular speed $\bar{c}_r$) (see Niemenen et al. [2010] for a similar modification). Many variables are then incorporated into a collision rate coefficient k_{GR}.

$$\frac{dD_p}{dt} = \frac{M_{SA}\alpha\bar{c}_r[SA^*]}{N_A 2w\rho}\left(1+\frac{d_{vapor}}{D_p}\right)^2 - \frac{D_p}{3}\frac{d\ln w\rho}{dt} \qquad \text{(S1)}$$

$$= k_{GR}[SA^*] - \frac{D_p}{3}\frac{\partial \ln w\rho}{\partial D_p}\frac{dD_p}{dt} - \frac{D_p}{3}\frac{\partial \ln w\rho}{\partial RH}\frac{dRH}{dt} \qquad \text{(S2)}$$

Here, D_p, w and ρ are the particle's diameter, SA (sulfuric acid) weight fraction, and density, respectively; M_{SA} is SA's molar mass, N_A is Avogadro's number, α and $\bar{c}_r$ are the mass accommodation coefficient of SA and mean molecular speed (using the reduced mass, taking into account hydration, Hanson and Eisele [2000]; about 2 water molecules at 52 % RH), [SA*] is the concentration of SA molecules and its hydrates, and d_{vapor} is the average diameter of hydrated SA molecules, 0.64 nm. Note that $\bar{c}_r$ calculated using the reduced mass of the particle-SA* collision for a particle diameter of 2.2 nm is only 1.35 % greater than the mean molecular speed of SA_1W_2. k_{GR} subsumes all the parameters besides [SA*] in the first term of the RHS of the top line.

$$k_{GR} = \frac{M_{SA}\alpha\bar{c}_r}{N_A 2w\rho}\left(1+\frac{d_{vapor}}{D_p}\right)^2 \qquad \text{(S2b)}$$

Solving for dD_p/dt for these conditions yields:

$$\frac{dD_p}{dt} = \frac{k_{GR}[SA^*] - \frac{D_p}{3}\frac{\partial w\rho}{\partial RH}\frac{dRH}{dt}}{1+\frac{D_p}{3}\frac{\partial \ln w\rho}{\partial D_p}} \qquad \text{(S3)}$$

The last term in the numerator is zero for experiments at constant RH and

$$\frac{dD_p}{dt} = \frac{k_{GR}[SA^*]}{1+\frac{D_p}{3}\frac{\partial \ln w\rho}{\partial D_p}} \quad \text{(S4)}$$

While k_{GR} accounts for uptake due to SA molecules it also accounts for water molecules taken up in addition to those attached to the SA molecule, determined by the nanoparticle's composition and density. The denominator accounts for additional water molecules taken up as the particle's composition changes with size. For the present conditions, this latter effect is about 8 % over the 3 to 8 nm range (i.e., the denominator is 0.92). See Table S2 below for representative values for the size dependent terms.

Splitting the growth from 2.2 to 8.7 nm into three time intervals Δt_i of 7.5 s to obtain an average value for k_{GR}/denominator of 3.38×10^{-11} nm cm^3/s, an average H_2SO_4 concentration is estimated from equation (S4)

$$[SA^*]_{ave} = 6.5 \text{ nm} / (22.5 \text{ s} * 3.38 \times 10^{-11} \text{ nm.cm}^3/\text{s}) = 8.55 \times 10^9 \text{ cm}^{-3}.$$

When the photolysis rate was set to 4.0×10^{-4} s^{-1}, the average on-axis [SA] calculated for these conditions (NO_x of 24.6 ppbv with 80 as HONO and 10 % for both NO and NO_2) is 8.56×10^9 cm^{-3}. The calculated profile is shown in Fig. 3 in the main paper and S11 below.

More rigorously, using the H_2SO_4 concentrations on-axis shown in Fig. S11 below (blue +) and calculating $\Delta D_p = \Sigma(dD_p/dt)_i \Delta t_i$ from i=1 to 3 using the values in rows 2, 3 and 5 in Table S2, we get an increase in diameter of 6.4 nm. This calculation also indicates that the growth experiments are consistent with a photolysis rate for HONO of 4×10^{-4} s^{-1}.

Table S2. Size dependent parameters in equation (S4). H_2SO_4 weight fraction is *w*, k_{GR} from eq. S2b. The calculation of ΔD_p: 7.5*(3.30e-11*1.077*2.4e9 +3.13e-11*1.094*8.7e9 + 3.08e-11*1.058*1.42e10).

D_p (nm)	*w*	° (g/cm^3)	*w*°	k_{GR} (10^{-11} nm cm^3/s)	1/denominator (S4)	Est. time (s)	Ave. $[H_2SO_4]$ / cm^{-3} In time interval
2.2	*0.58*	*1.47*	*0.85*	*3.44*		*0*	
3.3	0.54	1.44	0.78	*3.30*	1.077	*7.5*	*2.4e9*
5.0	0.51	1.40	0.71	3.13	1.094	15	8.7e10
7.7	*0.48*	*1.38*	*0.66*	*3.11*	*1.08*	*~19*	
8.7	0.47	1.375	0.65	3.08	1.058	22.7	1.42e10
10.0	*0.47*	*1.37*	*0.64*	*3.06*			

It is reasonable to suggest that a more appropriate measure of the particles' exposure to H_2SO_4 is the mixing-cup concentration: a flow-weighted average over the region sampled by the DEG system, 2 L/min. Assuming the DEG system samples the middle of the flow, this region covers radii from 0 to 1.4 cm. Shown in Fig. S10 are (a) the radial distributions of $[H_2SO_4]$ at four axial distances and (b) the mixing cup and on-axis $[H_2SO_4]$. Averaged from 0 to 120 cm, the mixing-cup concentration is about 10% less than the on-axis concentration. However, the flow slows with distance off centerline: for example, at 1 cm radius, the flow speed is 15 % less than on the centerline. This longer exposure time compensates somewhat for decreases in $[H_2SO_4]$ as R increases.

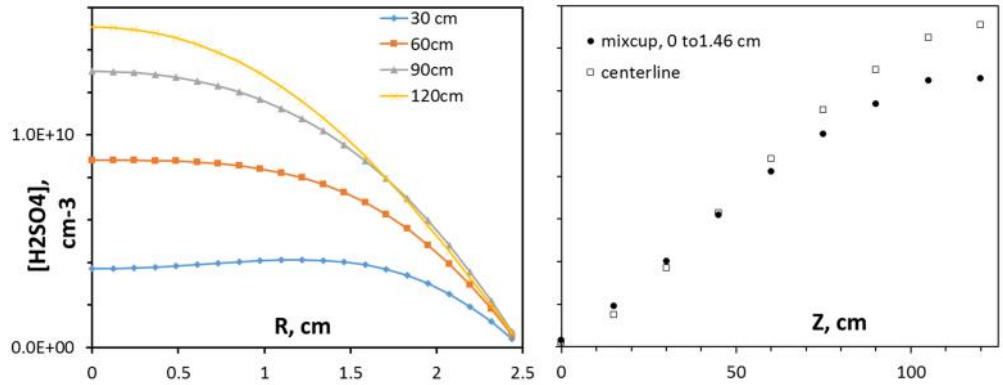

Fig. S10. Simulated [H_2SO_4] at Q_4 = 4.2 sccm. (a) Radial distributions at a few axial distances. Note that the data for Z = 120 cm is 11 cm beyond the simulation's lighted section. (b) Mixing-cup concentration and on-axis (centerline) concentrations plotted vs. axial distance.

S4. Previous determination of H_2SO_4 concentration: Photolysis rate, dependence on Q_4, etc.

Isoprene and methylvinylketone/methacrolein measurements were used to estimate the amount of HONO oxidized in our previous work [Hanson et al. 2019], however, the presence of 10 % NO was not considered. Again, the other differences are: (i) a level of 15 ppmv for the HCl-in-N_2 flow was estimated in our earlier work, (ii) also included was a reaction between HO_2 and SO_2 that yielded H_2SO_4 and an additional OH molecule and (iii) the HONO photolysis rate was larger. The HONO photolysis rate was estimated from absorption measurements along with isoprene photo-oxidation experiments, from the relative amount of methylvinylketone and methacrolein produced per isoprene lost. The precision of the absorption measurement was low yet the presence of NO_2 was posited, though not well quantified, due to HONO decomposition we believed to be take place in the absorption apparatus. Detection of NO was not attempted at that time. The presence of 10% NO is the reason for the large change in the estimate of the photolysis rate. The difference in the average H_2SO_4 between the simulation then and the present simulations is only 14 %, within the uncertainties of the measurements and in the branching ratios of isoprene's dominant photo-oxidation pathways.

S4.1 Calculated H_2SO_4 for previous conditions

The green asterisks in Fig. S11 are simulated H_2SO_4 using the previous parameters from Hanson et al. [2019]. These values differ from the present: 15 ppm HCl level in Q_4, no initial NO from the HONO generator, a photolysis rate of $8x10^{-4}$ s^{-1}, and a reaction between HO_2 and SO_2 was assumed to occur. The [H_2SO_4] averaged along the length of the reactor is $7.36x10^9$ cm^{-3}, about 14 % less than that of the current simulation (blue +).

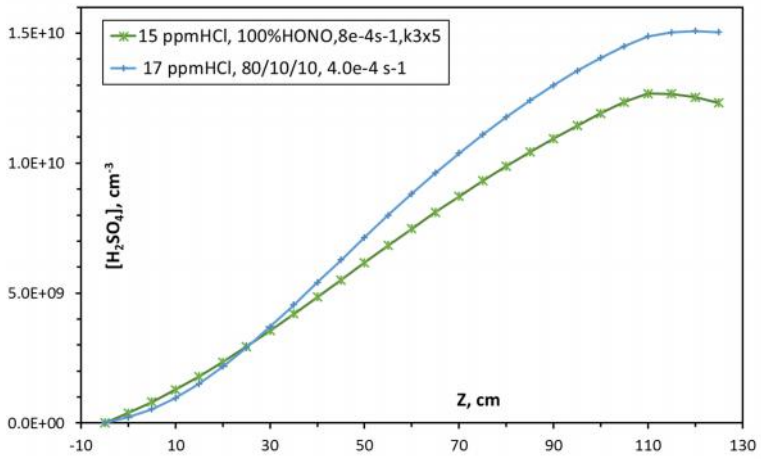

Fig. S11. Comparing Q_4 = 4.2 sccm on-axis H_2SO_4 concentrations simulated with previous parameters (green) [Hanson et al. 2019] and the present ones (blue) where NO_x is slightly enhanced, 10 % of that enters as NO and as NO_2, and there is no reaction for HO_2 with SO_2 (k3x5). The average on-axis [H_2SO_4] from Z=0 to 125 cm for these simulations are (blue) $8.56x10^9$ cm^{-3} and (green) $7.36x10^9$ cm^{-3}.

S5. Plots of modeled H_2SO_4 vs. experimental conditions.

Shown in Fig. S12 are simulated H_2SO_4 (on-axis values) at 60 cm and averaged over the length of the reactor plotted vs. Q_4 Both quantities are described well by a linear relationship however they have significant intercepts. That they are not strictly proportional to Q_4 is a consequence of changes in the [H_2SO_4] profiles with Q_4.

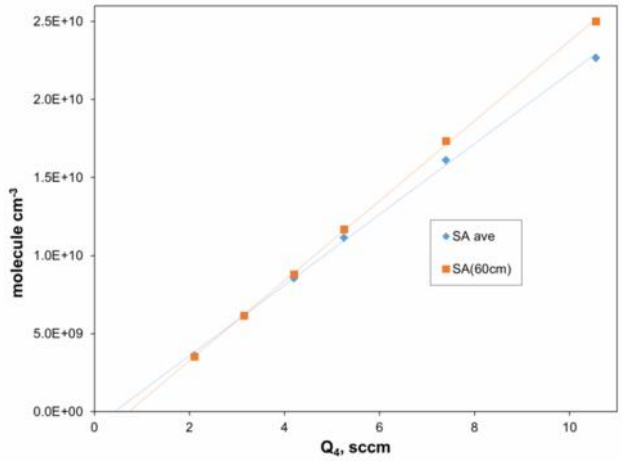

Fig. S12. Modeled on-axis [H_2SO_4] vs. Q_4/sccm. Average value over the length of the reactor and the H_2SO_4 concentrations at 60 cm are shown. The linear fits are $SA_{ave} = 2.26x10^9*Q_4 - 9.46x10^8$ and $SA(60cm) = 2.56*10^9*Q_4 - 1.83x10^9$ for SA in molecule cm^{-3} and Q_4 in sccm.

S6. Composition of the nano-particles.

We used the liquid drop model calculations of Lovejoy et al. [2004] to obtain the composition of aqueous sulfuric acid nano-droplets as a function of size for 296 K and 52 % RH. These are shown in Table S3 along with the 298 K and 50 % RH data from Fig. 2 of Yu [2005] for comparison. Note that bulk densities that corresponded to the composition of the nanoparticles were assumed to apply to the nanoparticles. The mass diameter is about 0.3 nm smaller than the mobility diameter according to Larriba et al. [2010].

Table S3. Compositions of H_2SO_4-H_2O clusters from SAWNUC [Lovejoy et al. 2004] and Yu [2005] for 52 % RH and 296 K. Bulk density ρ from CRC [1979], D_{mass} is mass diameter, k_f is the forward rate coefficient for addition of the doubly hydrated H_2SO_4 (SA) molecule indexed for product cluster. The volume of the clusters, V, as a function of # of SA molecules is given closely by: $V / cm^3 = 1.276x10^{-22}(\#SA)^{1.115}$.

# SA	Pk. # W SAWNUC[a]	Fastest SA evap.[b]	# W, Yu [c]	wt.%	° / (g/cm^{-3})[d]	D_{mass} / nm	k_f / cm^{-3} s^{-1}	k_f / cm^{-3} s^{-1} 'old' [e]	D_c / atm cm^2 s^{-1} [f]
1	1.5	-	1.2	78.4	1.71	**0.62**	-	-	0.076
2	4	2	3	73.1	1.65	**0.80**	3.88E-10	4.95E-10	0.057
3	7	4.5	5	71.5	1.63	**0.93**	4.39E-10	5.47E-10	0.0493
4	10.5	7.5	8.5	69.6	1.61	**1.04**	4.92E-10	6.02E-10	0.0418
5	14	10.5	11	67.7	1.58	**1.14**	5.43E-10	6.55E-10	0.0368
6	17.5	14	14	65.8	1.56	**1.22**	5.91E-10	7.03E-10	0.0330
7	21	17.5		64.5	1.55	**1.30**	6.37E-10	7.49E-10	0.0302
8	25	21	21	63.5	1.54	**1.37**	6.80E-10	7.93E-10	0.0279
9	28.5	25		62.8	1.53	**1.43**	7.22E-10	8.34E-10	0.0260
10	32	28.5	28	62.6	1.52	**1.49**	7.62E-10	8.74E-10	0.0244
20	74	70	65	59.5	1.50	**1.92**	1.11E-09	1.21E-09	0.0159
30	120	115	105	57.6	1.47	**2.23**	1.40E-09	1.47E-09	0.0123
40	168	163	170	56.4	1.45	**2.48**	1.66E-09	1.71E-09	0.0102
50	217	212	195	55.6	1.44	**2.69**	1.89E-09	1.91E-09	0.00883

100	479	474	420	53.2	1.42	**3.46**	2.90E-09	2.78E-09	0.00557
150	755			52.0	1.41	**4.00**	3.76E-09	3.48E-09	0.00424
200	1042			51.1	1.40	**4.44**	4.53E-09	4.09E-09	0.00348
300	1631			50.5	1.39	**5.13**	5.91E-09	5.16E-09	0.00263
∞	*#W / #SA = 7.5 in the bulk*			42.1	1.32	-	-	-	-

[a] Most abundant hydrate, pseudo-steady state. [b] Hydrate with the largest SA evaporation rate. [C] The critical cluster for 50 % RH and 298 K, from Yu's Fig 2(a). [d] CRC [1970] for the bulk densities. [e] 'old': Hanson et al. [2019] also used the kinetic theory of McMurry [1980] but assumed the monomer and all clusters had the bulk composition: 42 wt. % or 7.5 H_2O per H_2SO_4. [f] Diffusion coefficient using Mason and Monchick [1961,1962] with a collision integral factor ($\Omega_{1,1}$) = 1.24.

S7. Cluster model and thermodynamics

The two phenomenological sets of cluster free energies considered here differ in their putative binary system thermodynamics, our previous set, NH3_52 [Hanson et al. 2019], and the present set, NH3_D52. At the limit of zero NH_3 lie the binary system thermodynamics and these and those given by SAWNUC [Lovejoy et al., 2004, 2009] at 52% RH (transformed into quasi-unary by weighting over the water distribution to get an average equilibrium constant for addition of H_2SO_4) are compared in Fig. S13. Fig. S14 shows predicted N_p as a function of Q_4 for these three quasi-unary (zero ammonia) free energy schemes. NH3_52 and SAWNUC for 52 % RH yield N_p about one and two orders of magnitude greater than N_p for NH3_D52 which are close to the experimental data from Figure 5.

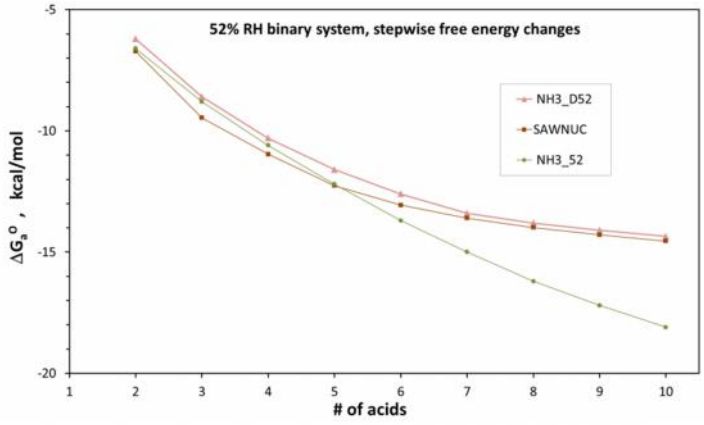

Fig. S13. Quasi-unary standard free energy changes for addition of H_2SO_4 (hydrated) to n-1 cluster as a function of product cluster, n. NH3_D52 is the binary set developed here, NH3_52 from Hanson et al. [2019] and SAWNUC is from Lovejoy et al. [2004].

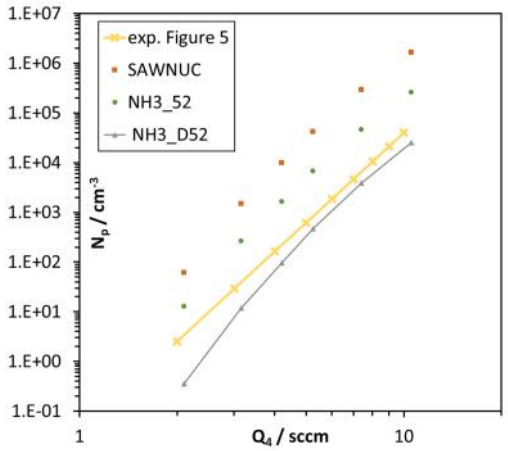

Fig. S14. Binary system, N_p vs. Q_4, modeled with three different thermodynamics. NO, NO_2 and HONO fractions were varied according to Figure 2. Thick yellow line represents lower envelope of data in Figure 5.

S7.1 NH3_D52 Gibbs energies and enthalpies for H_2SO_4-NH_3 clusters at 52 % RH.

Shown in Fig. S15 are the step-wise standard free energy changes for addition of an H_2SO_4 molecule, ΔG_a^0, for NH3_52 (thin lines) and NH3_D52 (thick lines). Product clusters are indexed with the number of H_2SO_4 molecules along the X-axis and number of ammonia molecules color-coded. These two schemes are close in ΔG_a^0 up to the 5 H_2SO_4 clusters; larger clusters (more NH_3 or more H_2SO_4) reveal that NH3_D52 has weaker bonding than does NH3_52, due in large part to the prescription that the large clusters with few ammonia molecules approach the quasi-unary free energy for the binary system.

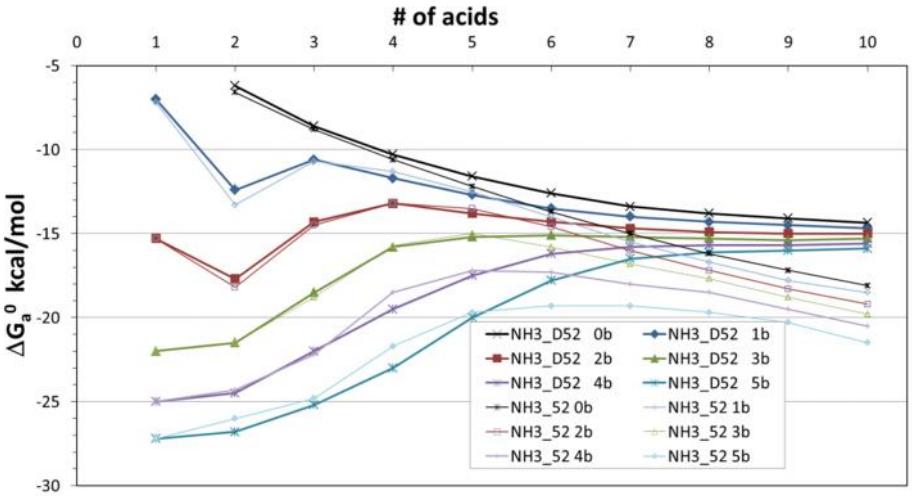

Fig S15. Comparison of NH3_D52 (thick lines) and NH3_52 (thin lines) thermodynamics, step-wise free energy changes for adding an acid molecule (binary is designated ' 0 b '). ΔG_a^0 for 1 acid binary is taken to be 0. The number of ammonia molecules in the cluster also indicated by color.

In the following tables, the free energies and enthalpies for NH_3-H_2SO_4 clusters at 53 % RH and 298 K are presented.

Table S4. Cluster Gibbs energies (298 K) as a function of # of sulfuric acids (columns) and # of ammonias (rows), kcal/mol.

	0	1	2	3	4	5	6	7	8	9	10
0	0	0	-6.2	-14.8	-25.1	-36.7	-49.3	-62.7	-76.5	-90.6	-104.95
1	0	-7	-19.4	-30	-41.7	-54.4	-67.9	-81.9	-96.2	-110.7	-125.4
2	4	-11.3	-29	-43.3	-56.5	-70.3	-84.6	-99.3	-114.2	-129.2	-144.2
3	8	-14	-35.5	-54	-69.8	-85	-100.1	-115.3	-130.6	-146	-161.3
4	9.5	-15.5	-40	-62	-81.5	-99	-115.2	-131	-146.7	-162.4	-178
5	10.7	-16.5	-43.3	-68.5	-91.5	-111.5	-129.3	-145.8	-161.9	-177.9	-193.8
6	11.9	-17.5	-46	-73.6	-99	-121.9	-142	-159.8	-176.7	-193	-209.3

Table S5. Enthalpies (kcal/mol) as a function of # of sulfuric acids (columns) and # of ammonias (rows)

	0	1	2	3	4	5	6	7	8	9	10
0	0	0	-16.3	-37.3	-59.8	-83.8	-108.8	-134.8	-161.8	-189.8	-218.8
1	0	-14	-40	-63.5	-87	-111	-136	-162.0	-189.0	-217.0	-246.0
2	0.4	-26	-57	-86	-112	-137	-163	-189.5	-217.0	-245.5	-275.0
3	-4.4	-36	-73	-106.5	-136	-161	-187	-215.0	-244.0	-272.5	-302.0
4	-8.3	-46.3	-85	-122	-156	-183	-210	-238.0	-267.0	-297.0	-327.0
5	-12.2	-53	-94	-134	-171	-203	-232	-261.0	-291.0	-321.0	-352.0
6	-16.1	-59.5	-101.5	-144	-183	-220	-252	-282.0	-313.0	-344.0	-376.0

S8. Ion calculations and discussion.

The Froyd et al. data covers up to 6 H_2SO_4 ligand molecules on the bisulfate ion and also has energetics of hydration. We averaged over hydrates to obtain a quasi-unary equilibrium constant that yields the free energies for the negative ions.

The forward rate coefficient was taken to be $2x10^{-9}$ cm^3 s^{-1} for all clusters. The quasi-unary free energies were extended to 9 H_2SO_4 ligands by assuming no changes in the stepwise ΔG. In the ion-mediated pathway, particles can also be formed when positive and negative ions recombine but for our conditions this was found to be negligible compared to the negative ion channel. Experimentally, these ions / charged particles will be affected / neutralized in the charger which will affect how the DEG system counts them while the UCPC system counts them regardless. The quasi-unary free energies for the negative ions are presented in Table S6.

Table S6. Quasi-unary Gibbs energies at 296 K and 52% RH. Ion energies from Froyd et al. SAWNUC (modified liquid drop) energies from Lovejoy et al. [2004]. n is that in (HSO_4^-). $(H_2SO_4)_n$ or $H_2SO_4.(H_2SO_4)_n$.

n, # of H_2SO_4 ligands	aG^0, SAWNUC stepwise	Total standard free energy	Stepwise, bisulfate ion, Froyd et al.	Total, ion
0	-	0	-	-
1	-6.72	-6.72	-23.02	-23.02
2	-9.46	-16.17	-17.03	-40.05
3	-10.96	-27.14	-13.84	-53.88
4	-12.26	-39.40	-11.70	-65.58
5	-13.06	-52.46	-12.62	-78.20
6	-13.60	-66.06	-13.08	-91.28
7	-13.99	-80.04	-13	-104.28
8	-14.29	-94.33	-13	-117.28
9	-14.54	-108.88	-13	-130.28

References not in main text:

Handbook of Chemistry and Physics, 35th edition, Hodgman, C.S., Weast, R.C., Wallace, C.W. editors, Chemical Rubber Publishing Co., Clevelend, OH, 1953-1954.

Kangasluoma, J., C. Kuang, D. Wimmer, M. P. Rissanen, K. Lehtipalo, M. Ehn, D. R. Worsnop, J. Wang, M. Kulmala, T. Petäjä: Sub-3 nm particle size and composition dependent response of a nano-CPC battery, Atmos. Meas. Tech., 7, 689–700, 20141 www.atmos-meas-tech.net/7/689/2014/ doi:10.5194/amt-7-689-2014

Larriba, A., Hogan, C. and de Lamora, J.: The Mobility–Volume Relationship below 3.0 nm Examined by Tandem Mobility–Mass Measurement, Aerosol Science and Technology, 45, 453-467, 2010.

Monchick, L.; Mason, E. A. The Transport Properties of Polar Gases. J. Chem. Phys. 1961, 35, 1676.

Mason, E. A.; Monchick, L. Transport Properties of Polar-Gas Mixtures. J. Chem. Phys. 1962, 36, 2746.

Nieminen, T., Lehtinen, K. E. J. and Kulmala, M.: Sub-10 nm particle growth by vapor condensation – effects of vapor molecule size and particle thermal speed, Atmos. Chem. Phys., 10(20), 9773–9779, doi:10.5194/acp-10-9773-2010, 2010.